ADVANCED MATERIALS
www.advmat.de

Memristive Behavior Enabled by Amorphous–Crystalline 2D Oxide Heterostructure

*Xin Yin, Yizhan Wang, Tzu-hsuan Chang, Pei Zhang, Jun Li, Panpan Xue, Yin Long, J. Leon Shohet, Paul M. Voyles, Zhenqiang Ma, and Xudong Wang**

The emergence of memristive behavior in amorphous–crystalline 2D oxide heterostructures, which are synthesized by atomic layer deposition (ALD) of a few-nanometer amorphous Al_2O_3 layers onto atomically thin single-crystalline ZnO nanosheets, is demonstrated. The conduction mechanism is identified based on classic oxygen vacancy conductive channels. ZnO nanosheets provide a 2D host for oxygen vacancies, while the amorphous Al_2O_3 facilitates the generation and stabilization of the oxygen vacancies. The conduction mechanism in the high-resistance state follows Poole–Frenkel emission, and in the the low-resistance state is fitted by the Mott–Gurney law. From the slope of the fitting curve, the mobility in the low-resistance state is estimated to be ≈2400 $cm^2 V^{-1} s^{-1}$, which is the highest value reported in semiconductor oxides. When annealed at high temperature to eliminate oxygen vacancies, Al is doped into the ZnO nanosheet, and the memristive behavior disappears, further confirming the oxygen vacancies as being responsible for the memristive behavior. The 2D heterointerface offers opportunities for new design of high-performance memristor devices.

The increasing demand of high density, non-volatile memory devices has been driving the development of nanoscale memory-bit cells.[1] First proposed by Chua et al.,[2] the memristor was realized in the form of metal-insulator-metal (MIM) heterostructures in which the electrical resistance of the insulator could be switched by applied electrical bias. This simple structure offers a promising solution for high-density data storage. The electrically switched on-off behavior also has great promise as the artificial neuron synapses for neuromorphic computing.[3] A large class of materials have been studied as the memristive material, including metal oxides,[4] halides,[5] chalcogenides,[6] colloidal suspensions[7] and organic polymers.[8] Among them, metal oxides are the most intensively investigated due to their good chemical stability and broad selection of electrical properties. In particular, ZnO thin films have attracted great interest due to their facile preparation approaches, excellent compatibility for device integration, and controllable electronic and optoelectronic behavior.[9] Their memristive behavior is primarily associated with the non-equilibrium distribution of oxygen vacancies in response to an external electrical field. This switching mechanism allows robust cycling endurance, but it is always associated with low switching speed.[10] In contrast, 2D nanomaterials offer a quantum-confined medium which can have exceptional transport properties and substantially improved memristive behavior compared to conventional bulk materials. For example, single atomic layer 2D transition metal dichalcogenide memristors exhibited high-frequency switching with an extremely low power consumption,[6,11] and memristors based on ultrathin single-crystalline SiGe layer demonstrated significantly improved reproducibility and low energy consumption.[3] Developing memory devices with low operating voltages and low energy consumption go in the direction of a connection between instrinsically neuromorphic devices and living neurons.[12] Nevertheless, due to the unavailability of 2D oxides nanomaterials and the high entropy of introducing vacancies in 2D confined geometry, stable 2D oxide-based memristors have yet to be demonstrated.[9]

Recently, ionic layer epitaxy (ILE) was developed as a versatile solution-based approach for growing large-area oxide nanosheets on a liquid surface.[13] Atomically thin single-crystalline ZnO nanosheets were synthesized with sizes over 10 µm, enabling the study of the memristor properties based on 2D metal oxides. In this work, we show extraordinary memristive behavior enabled by interfacing atomically thin single crystalline ZnO nanosheets with a few-nm thick amorphous Al_2O_3 layer. The conduction mechanism was attributed to the classic oxygen vacancy conductive channels in the lateral transistor module. In this configuration, the ZnO nanosheet provides a 2D host of oxygen vacancies, while the amorphous Al_2O_3 facilitates the generation and stabilization of the oxygen vacancies. The 2D heterointerface brought a new promise for flexible non-volatile and ultralow power memory devices.

Atomically thin single-crystalline ZnO nanosheets were synthesized by ILE,[13,14] in which amphiphilic molecules (oleyl sulfate) self-assembled into a monolayer at the water–air

Dr. X. Yin, Dr. Y. Wang, Dr. P. Zhang, J. Li, Dr. Y. Long, Prof. P. M. Voyles, Prof. X. Wang
Department of Materials Science and Engineering
University of Wisconsin-Madison
Madison, WI 53706, USA
E-mail: xudong.wang@wisc.edu
Dr. T.-h. Chang, Dr. P. Xue, Prof. J. L. Shohet, Prof. Z. Ma
Department of Electrical and Computer Engineering
University of Wisconsin-Madison
Madison, WI 53706, USA
The ORCID identification number(s) for the author(s) of this article can be found under https://doi.org/10.1002/adma.202000801.

DOI: 10.1002/adma.202000801

interface, serving as a template to direct the nucleation and growth of ZnO crystalline nanosheet underneath. The as-synthesized ZnO nanosheet with a size up to ≈10 µm was then transferred onto a Si wafer with 50 nm thermal oxide layer for device fabrication. All the as-transferred nanosheets displayed a well-developed triangular shape without any observable wrinkles or overlap (Figure S1a, Supporting Information), and thus were ready for device processing. Ti/Au electrodes were deposited onto ZnO nanosheets by e-beam evaporation to form lateral Ti/Au–ZnO–Ti/Au (MIM) devices (**Figure 1**a; Figure S1d, Supporting Information). Owing to the relatively uniform distribution and large coverage of ZnO nanosheets, no pre-alignment was needed for electrodes and >50% were connected to form a functional device. The MIM structure had a wide space (≈3 µm) between the two electrodes, where the thickness of the uncoated nanosheet channel was only ≈0.75 nm as probed by an AFM scan (Figure 1b,c). This thickness roughly corresponded to one unit cell of wurtzite ZnO. The Ti/Au electrodes were measured to be ≈43 nm thick (Figure S1f, Supporting Information). When sweeping the voltage from −15 to 15 V, ZnO nanosheets behaved as an insulator (Figure S2a, Supporting Information). This result was expected because when a bulk material is downsized to atomically thin dimensions, a strong correlation between the surface states (or traps) and charge carriers would significantly impair the mobility of free charges.[15] It has also been reported that the band gap of atomically thin ZnO increases up to 4.0 eV, becoming more insulating.[16]

A 5 nm thin amorphous Al_2O_3 layer was then deposited on the surface of the entire ZnO nanosheet device by atomic layer deposition (ALD), as schematically shown in Figure 1a (also see Figure S3 in the Supporting Information). Due to the conformal coverage of the ALD film, the height profile of the coated device was not observably different from the profile of the

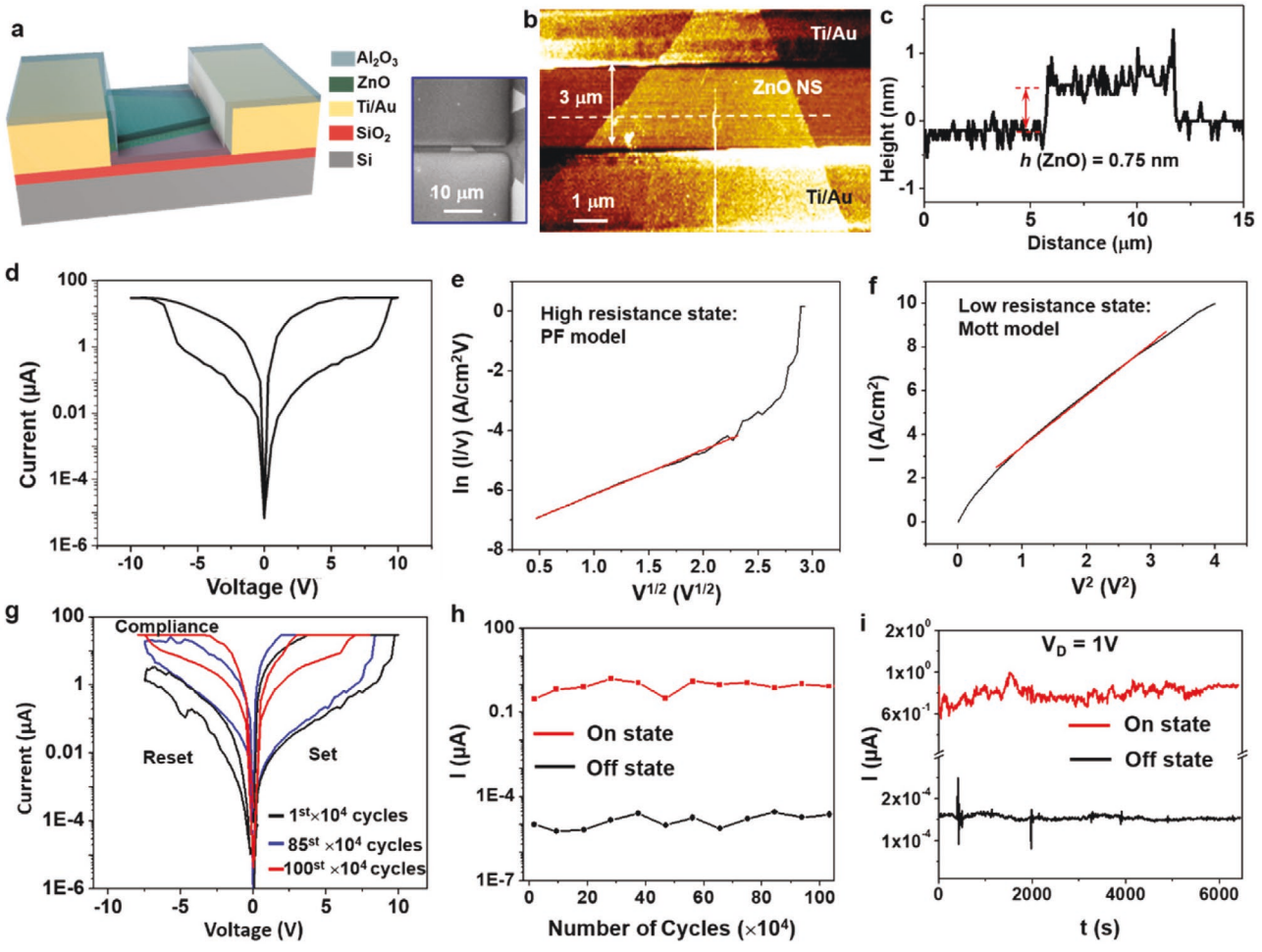

Figure 1. ZnO/Al_2O_3 memristive device characterization. a) Schematic of a ZnO/Al_2O_3 heterolayered nanosheet memristor. Inset: SEM image showing a conductor-oxide-conductor memristor consisting of two electrodes bridged by one nanosheet. b) AFM topography image illustrating the channel width and length of one typical memristor. c) Height profile showing the thickness of the nanosheet in (b) was 0.75 nm. d) The logarithm scale of the *I*–*V* curve of ZnO/Al_2O_3 memristor. e) Fitting curve at the HRS portion showing the Poole–Frenkel emission model as the conduction mechanism. f) Fitting curve at the LRS portion showing Mott–Gurney behavior as the conduction mechanism. g) Three *I*–*V* curves of the ZnO nanosheet memristor at the 1×10^4th cycle, 85×10^4th cycle, and 100×10^4th cycle, showing the sustained memory behavior throughout a large number of cycles. h) The endurance of one device over 10^6 cycles at "On" and "Off" states respectively. ≈500 ns pulses were used for the device measurement. i) The retention of the "On" and "Off" states over 100 min. A read voltage of 1 V was used for the measurement.

uncoated device. The ALD-coated ZnO nanosheets exhibited a strong memristive behavior when the voltage was swept between ±10 V (Figure 1d). Starting at 0 V, the device exhibited the high-resistance state (HRS) with a very low current at the level of nA. As the voltage increased to ≈8.75 V, the current abruptly jumped to above μA, switching to the low-resistance state (LRS), i.e., the set process. This bipolar behavior could be attributed to the largely different ZnO channel width between the two electrodes (Figure 1b). The observed current saturation at 30 μA was a result of the compliance to prevent the device from electric breakdown due to the ultrahigh current in the LRS. The device stayed at the LRS when the voltage was swept back to 0 V. In the negative bias sweep, the device began with the LRS and then changed back to the HRS at ≈−7.44 V. This relatively large applied voltage was due to the large electrode distance (3 μm). Given the fact that the set voltage is directly proportional to the electrodes distance,[17,18] the V_{set}/V_{reset} could be reduced to the mV level when the distance was decreased to tens of nanometers with advanced fabrication technology. Only Al_2O_3 ALD-coated ZnO nanosheets exhibit the memristive hysteresis loop; while bare nanosheets do not. Besides, no forming process was needed in the ZnO/amorphous Al_2O_3 memristors. This was because a large amount of oxygen vacancies was formed in ZnO after Al_2O_3 ALD coating, which brought the resistance of the as-fabricated device close to the reset state.[19] Control experiments showed that neither the substrate nor amorphous Al_2O_3 without ZnO exhibit memristive behavior (Figures S2 and S4, Supporting Information).

The conduction behavior at HRS and LRS was analyzed to understand the memristive mechanism in the 2D heterosystem. The *I*–*V* curve within the HRS range from 0 to 6.25 V was fitted. As shown in Figure 1e, by plotting ln*J* as a function of $V^{1/2}$, the transport characteristic fitted well to the Poole–Frenkel emission model within the voltage range between 0.5 and 2.5 $V^{1/2}$ following the equation[20]

$$J \cong V \exp\left(\frac{q}{kT}\left(\sqrt{qV/4\pi\varepsilon_r\varepsilon_0 d} - \phi_B\right)\right) \quad (1)$$

where q is the electron charge, k is the Boltzmann constant, d is the distance between electrodes, ε_r is the relative permittivity, ε_0 is the permittivity of free space, ϕ_B is the barrier height, and T is absolute temperature. The *I*–*V* curve within the HRS range does not fit the hopping conduction model. Therefore, the conduction mechanism at the HRS could be attributed to charge emission from traps to the conduction band under high electric fields, which is a normal conduction mechanism in insulators. At a higher voltage range (>6.25 V), the curve deviated from the Poole–Frenkel emission model. This is possibly due to the state transition from HRS to LRS, as the set process started at ≈8.75 V. The LRS *I*–*V* characteristic was fitted from 4 to 1 V^2 when the applied voltage was swept back to 0 V. The transport behavior fitted well with the Mott–Gurney law[21] (Figure 1f), following the relation

$$I = \frac{9}{8}\varepsilon_r\varepsilon_0\mu\frac{V^2}{d^3} \quad (2)$$

where μ is the carrier mobility. The Mott–Gurney behavior describes the charge transport as a result of the drifting of the charge carriers along the direction of the electric field. The Mott–Gurney fitting indicated that the LRS at 1–2 V was mainly controlled by space charge limited conduction (SCLC). In the SCLC mechanism, the current flow in the LRS is governed by oxygen vacancies, which form a conductive filament between the electrodes.[22,23] In addition, according to the fitting curve, the carrier mobility was estimated to be ≈2400 $cm^2\ V^{-1}\ s^{-1}$, by using $\varepsilon_r = 8.5$ and $d = 3$ μm. This value is the highest reported carrier mobility in semiconductor oxides (Table S1, Supporting Information).[24] The drift velocity (v) can be estimated using the equation: $v = \mu E$, where "E" is the electric field, and μ is carrier mobility.[25] When the applied voltage was 2 V, the drift velocity was estimated to be 1.6×10^5 m s^{-1}, which was comparable to the electron thermal velocity in Si (2.3×10^5 m s^{-1}).

Repeatability was studied through setting/resetting the device by pulse cycles for up to × 10^6 times (Figure 1g; Figure S5, Supporting Information). The blue curve and the red curve in Figure 1g represent the 8.5×10^5th cycle and 1×10^6th cycle, respectively. By increasing the cycle number, both the set and reset voltages decreased. The set voltage decreased to 7.56 and 5.88 V at the 8.5×10^5th and 1×10^6th cycles, while the reset voltage became −6.84 and −6.32 V, respectively. The resistance of both the LRS and HRS also decreased gradually in the negative bias sweep. However, except for these observations, the similar characteristic hysteresis loops indicate that the memristive behavior remained repeatable for 10^6 cycles. The current at the LRS and HRS extracted from different pulse cycles showed good endurance (Figure 1h), comparable to the typical endurance of commercial flash memories.[26] Retention is another important criterion, which was evaluated by respectively measuring the current at a sustained voltage of 1 V after setting the devices at LRS and HRS. As shown in Figure 1i, the current was stable at 0.28 mA mm^{-1} at HRS and 5.42×10^{-5} mA mm^{-1} at LRS for 100 min without degradation. Major parameters extrapolated from our memristor are summarized in **Table 1**. Compared to various memristive structures based on ZnO,[27] our device showed an endurance among the highest values (10^6), while maintaining a large ON/OFF ratio and good retention performance. Most importantly, our device was able to reset at a low current (0.03 mA) and switch between HRS and LRS at low electric field (2.9×10^6 V m^{-1}), suggesting a good potential to achieve low power consumption. In contrast, most ZnO-based memristive devices exhibited high power consumption as a result of the high operation current (>mA).[27]

In order to understand the influences of the amorphous Al_2O_3 coating on the emergence of the memristive behavior, the crystal structure before and after the amorphous Al_2O_3 coating was investigated. The low-magnification STEM image in **Figure 2**a showed an as-synthesized triangular ZnO nanosheet (with brighter contrast) resting on a holey carbon TEM grid. The high-resolution TEM (HRTEM) image in Figure 2b reveals the single-crystalline lattice with a typical hexagonal arrangement. The selected area electron diffraction (SAED) in the inset of Figure 2b confirmed the wurtzite crystal structure with the surface in the (0001) plane. Then, a 2 nm amorphous Al_2O_3 layer was uniformly deposited on the nanosheet sample by ALD. Figure 2c shows that the morphology of the triangular nanosheet after Al_2O_3 coating was well maintained. The single-crystalline wurtzite crystal lattice also was well preserved

Table 1. Comparison of the memristive performance of ZnO structures.

structure	Electrodes distance	Maximum operation current [mA]	V_s [V]	V_R [V]	Electric field [$\times 10^7$ V m^{-1}]	Endurance [cycles]	ON/OFF ratio [times]	Retention [s]	Year	Ref.
Pt/ZnO/Pt	100 nm	30	−2	−1	−2	100	10^3–10^4	NA	2008	[20b]
Pt/ZnO/Pt	25 nm	3	1.2	−0.5	4.8	10^6	>100	$>6\times10^5$	2012	[34]
Pt/ZnO/Ru	85 nm	10	1.9	0.7	2.2	200	175	9×10^4	2011	[35]
TiN/ZnO/Pt	30 nm	5	1.2	−1.2	4	>500	10	NA	2008	[36]
Au/ZnO/ITO	20 nm	40	2	−2	10	>100	>10	10^4	2011	[37]
Al/ZnO/Al	70 nm	1	2.5	0.5	3.6	219	10^4	10^3	2015	[38]
TiN/ZnO/TiN	40 nm	80	−4	3	−10	NA	>10	10^4	2016	[39]
Pt/V-ZnO/Pt	250 nm	10	−2.5	−0.5	−1	10^5	10^2	3.6×10^4	2014	[40]
Al/Al_2O_3/$(ZnO/Al_2O_3)_{10}$/n-Si/Al	118 nm	0.05	7	−7	5.9	NA	10^3–10^4	10^3	2015	[41]
Al/ZnO/Al	60 nm	0.1	−6.2	6.3	10	250	10	10^6	2017	[42]
Al/ZnO/p+-Si	38 nm	0.1	2.2	−2.5	5.8	NA	NA	NA	2017	[43]
Cu/ZnO/Pt	100 nm	80	1	−1.5	1	100	10	NA	2018	[44]
Au/ZnO/Pt	200 nm	0.01	3	−0.5	1.5	300	10	10^3	2018	[45]
Mg/ZnO/W	100 nm	≈12	1.5	−1	1.5	140	≈10^4	10^4	2018	[46]
Cu/ZnO/ITO	14 nm	70	1	−1.7	7	100	10	NA	2019	[47]
Au/ZnO/Al_2O_3/Au	3 µm	0.03	8.75	−7.44	0.29	10^6	10^3	6×10^3		This work

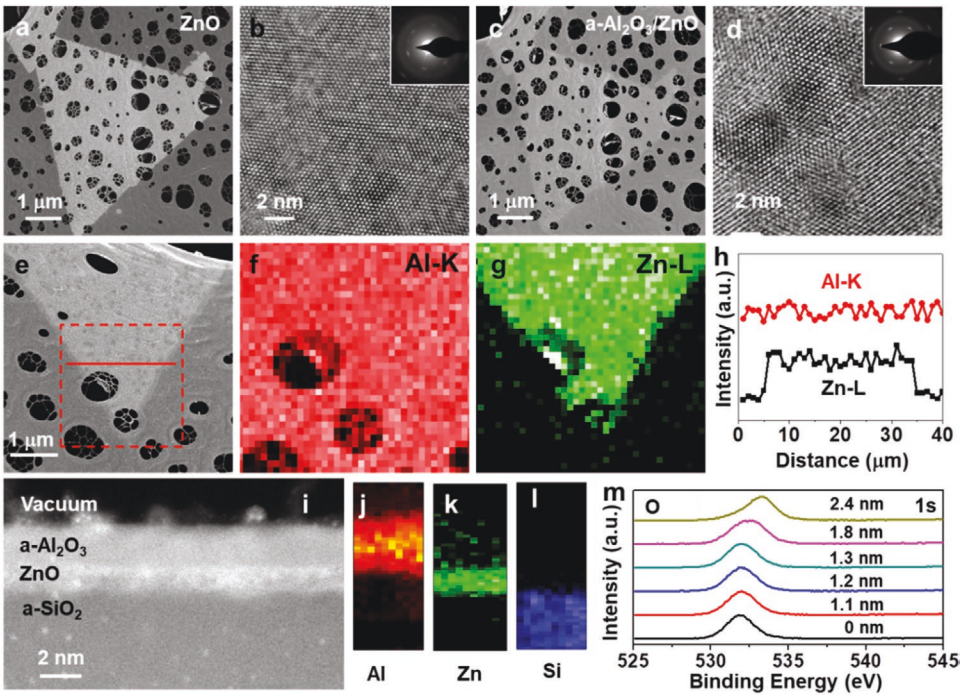

Figure 2. Crystal structure characterization of ZnO and ZnO/Al_2O_3 nanosheets. a) Low-magnification STEM image of one ZnO nanosheet resting on a TEM grid. b) High-resolution TEM image showing the crystal lattice of wurtzite ZnO, viewed on the [0001] zone axis. Inset is the selected-area electron diffraction (SAED) pattern confirming the single-crystalline wurtzite structure. c) Low-magnification STEM image of one ZnO nanosheet coated by an amorphous Al_2O_3 layer on a TEM grid. d) High-resolution TEM image showing of the wurtzite crystal lattice of ZnO nanosheet, indicating the ZnO nanosheet was not impaired by the Al_2O_3 deposition. Inset is the SAED pattern. e) Low-magnification STEM image and f,g) corresponding EDS elemental mapping of aluminum (f) and zinc (g) in the area marked by the red dashed box in (e). h) Al and Zn element intensity profile along the red solid line in (e). i) Cross-section STEM image of one memristor device showing the stacking of the ZnO nanosheet and the amorphous Al_2O_3. j–l) The corresponding element mapping of Al (j), Zn (k), and Si (l) showing that each layer had a distinct area and there was no observable interaction among them. m) Depth-profiling X-ray photoelectron spectroscopy of one memristor device, showing the oxygen peak shifted from 531.9 eV in Al_2O_3 to 532.4 eV in ZnO, and to 533.3 in SiO_2.

after the coating (Figure 2d), and the sharp SAED pattern in the inset of Figure 2d further confirmed no other crystalline phase was introduced by ALD. Energy-dispersive X-ray spectroscopy (EDS) mapping was employed to investigate the elemental distribution. EDS mapping at the corner area marked by the red dashed box in Figure 2e showed a universal distribution of Al (Figure 2f) and a well-defined triangular distribution of Zn (Figure 2g). The line profiles of Al and Zn along the red solid line in Figure 2e also exhibited a good match across the entire nanosheet (Figure 2h). The STEM image in Figure 2i is a cross-section through the heterojunction, showing three distinct layers of thick amorphous SiO_2, ≈1 nm ZnO, and ≈2 nm amorphous Al_2O_3. The corresponding element maps confirmed the well separated layers of Al (Figure 2j), Zn (Figure 2k), and Si in SiO_2 (Figure 2l). The depth profile from X-ray photoelectron spectroscopy (XPS) was obtained by etching away the materials layer-by-layer through Ar sputtering with a depth resolution of ≈0.2 nm. As shown in Figure 2m, at the beginning (the top surface), the oxygen signal mainly came from Al_2O_3, with a position of 531.9 eV. By etching away the materials layer by layer, the oxygen peak gradually shifted to 532.4 eV at the depth of 1.8 nm and to 533.3 eV at the depth of 2.4 nm. This result matched well with layer configuration (Al_2O_3/ZnO/SiO_2).[13] All these characterizations verified that the amorphous–crystalline interface was formed by ALD deposition, without Al doping into ZnO lattice or chemical reaction between ZnO and Al_2O_3.

Electron energy loss spectroscopy (EELS) results from cross section samples shown in **Figure 3** confirm that the Al_2O_3 coating induces O vacancies in the ZnO nanosheet. Figure 3a is the O K-edge from uncoated ZnO, with a narrow peak (Peak A) at 537.8 eV and a broad peak (Peak B) at 556.2 eV. Figure 3b is the Zn L-edge from uncoated ZnO, with a broad peak typical of ZnO and a small shoulder at 1024.2 eV. The Zn:O ratio derived from these data is 1.10 ± 0.11, so the uncoated sheet may be slightly O-poor, but is within experimental uncertainty of stoichiometric. Figure 3c,d are the O and Zn edges,

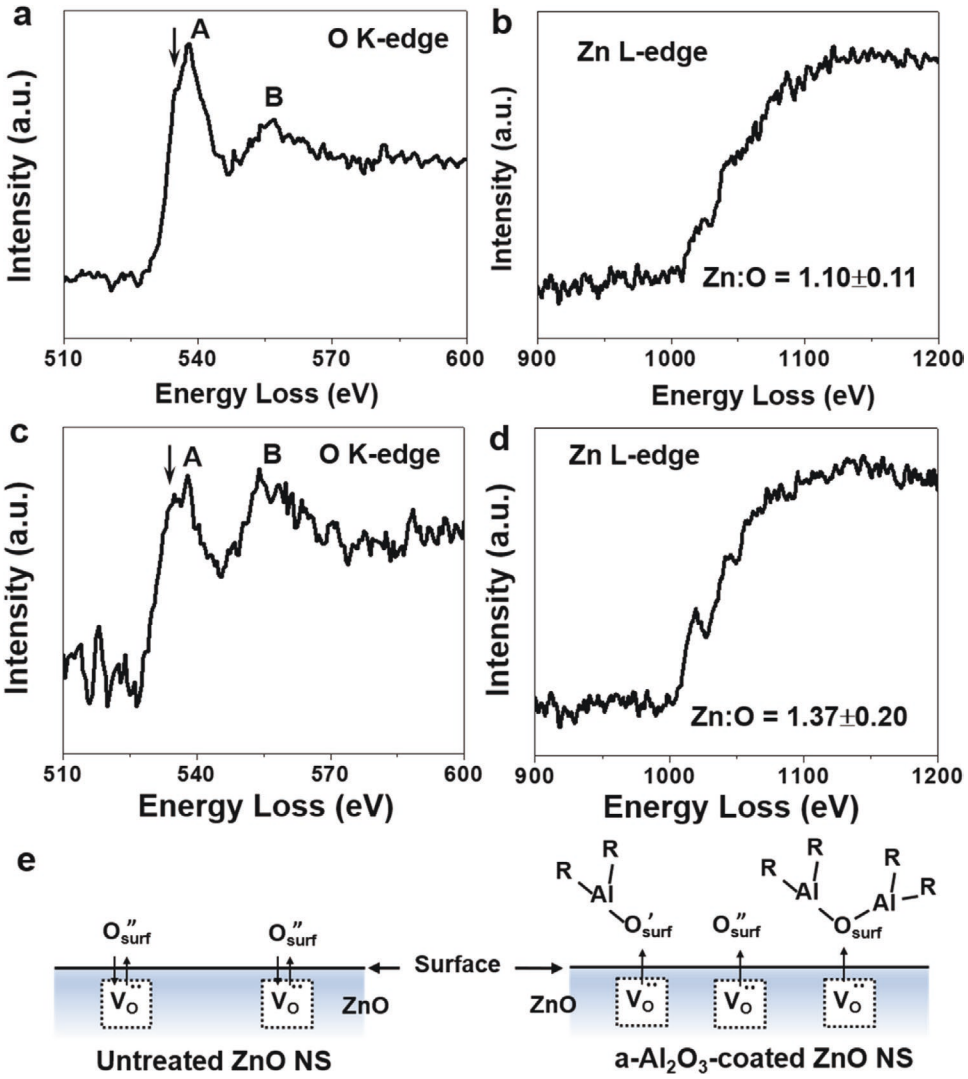

Figure 3. Mechanism study of oxygen vacancy formation. a–d) Electron energy loss spectroscopy on cross section samples comparing the O K-edge (a) and Zn L-edge (b) from base ZnO nanosheets to the O K-edge (c) and Zn L-edge (d) from amorphous Al_2O_3 coated ZnO nanosheets. e) The proposed mechanism for the evolution of high-concentration oxygen vacancies as a result of Al_2O_3 ALD.

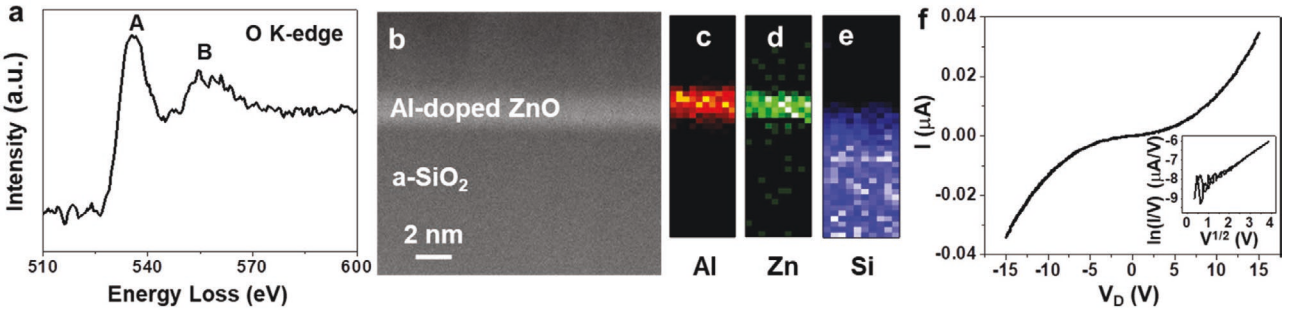

Figure 4. Control to confirm the critical role of Al_2O_3/ZnO heterostructure. a) EELS O K-edge peak of annealed a-Al_2O_3/ZnO nanosheets. b) Cross-section STEM image of an annealed a-Al_2O_3/ZnO nanosheet on SiO_2. c–e) Corresponding cross-sectional element mapping of Al (c), Zn (d), and Si (e). f) *I–V* curve measured from the transistor made from an annealed a-Al_2O_3/ZnO nanosheets showing the non-hysteresis transport property. Inset: fitting curve showing the conduction behavior matched well with Poole–Frenkel emission mode.

respectively, from an Al_2O_3-coated ZnO nanosheet. The Zn:O ratio is 1.37 ± 0.20. The composition suggests a large concentration of O vacancies, which is confirmed by the fine structure. The O K-edge develops a significantly more intense low-energy shoulder to peak A at 534.9 eV, and the Zn L-edge shoulder at 1024.2 eV becomes a distinct pre-peak. Both features are characteristic of O vacancies in ZnO.[28]

The formation of the oxygen vacancies as a result of Al_2O_3 coating is proposed in Figure 3e. For typical ZnO crystals, O Frenkel defects are usually present.[29] Near the surface, O ions move to the surface and leave the bulk lattice concentrated with oxygen vacancies, i.e., $O_O^x \rightarrow V_O^{\cdot\cdot} + O''_{surf}$. We expect similar behavior in situation for our as-synthesized ZnO nanosheets. When the Al precursor (trimethylaluminum, TMA) is introduced to the ZnO nanosheets during ALD, it preferably bonds to the surface O ions, as the bonding energy of Al—O (511 kJ mol^{-1}) is significantly larger than that of Zn—O (159 kJ mol^{-1}).[30] The consumption of surface O ions by the precursor further drives the surface Frenkel reaction to the right hand side and yields more oxygen vacancies near the surface region. Such oxygen extraction reaction has also been observed from the ALD reactions of TMA with other ZnO structures.[30,31] Due to the ultrasmall thickness of our ZnO nanosheets, this surface effect would turn into a bulk property and fill the entire ZnO channel with concentrated O vacancies. Under an in-plane electric field, these O vacancies were able to diffuse and cluster together,[32] forming continuous conductive filaments to carry a high electric current in between the two electrodes (Figure S7, Supporting Information). Hence, the O vacancy-related memristive behavior could be significantly enhanced in this unique amorphous Al_2O_3–ZnO nanosheet heterostructure.

To further verify that the oxygen vacancies' contribution to the memristive behavior, the heterojunction was annealed in air at 500 °C for 1 h, to remove the oxygen vacancies and drive Al into the ZnO lattice. O K-edge EELS on the annealed sample shows the characteristic peaks A and B, but the shoulder at 534.9 eV is suppressed, indicating the quantity of oxygen vacancies was largely reduced (**Figure 4**a). The cross sectional STEM image in Figure 4b shows that the Al_2O_3 layer and ZnO nanosheet have mixed together and sit on the SiO_2 substrate, as do the Al, Zn, and Si EDS maps in Figure 4c–e. The Al doped ZnO nanosheets showed good conductivity due to the increased free electrons created by Al doping (Figure 4f).[33] The conduction mechanism fitted well with Poole–Frenkel emission mode (inset of Figure 4f). As expected, no memristive behavior was observed from the *I–V* characteristics. This result confirmed our assumption that the memristive behavior was produced by the high switching speed in the presence of an electric field.

In conclusion, we have observed high on/off ratio, easily set and reset, high-endurance memristive switching in heterostructures consisting of atomically thin ZnO coated with amorphous Al_2O_3 by ALD. As-synthesized ZnO nanosheets behaved as insulators. The Al_2O_3 coating dramatically enhanced the transport behavior and created memristive behavior. The conduction mechanism followed Poole–Frenkel emission in the HRS and the Mott–Gurney law in the LRS. From the slope of the fitting curve, the mobility and the drifting velocity in the LRS were estimated to be ≈2400 $cm^2\ V^{-1}\ s^{-1}$ and 1.6×10^5 m s^{-1}, respectively. This performance is superior to all other reported ZnO memristors, particularly the considerably lower reset current and switching electric field. The memristive behavior arises from high-speed drift of oxygen vacancies in the ZnO created by the Al_2O_3. The presence of O vacancies is confirmed by materials characterization of the heterostructures, and their role in switching is confirmed by the absence of switching in an annealed heterostructure. This discovery suggests a new route for realizing high-performance memristor devices using 2D oxide heterostructures.

Supporting Information

Supporting Information is available from the Wiley Online Library or from the author.

Acknowledgements

X.Y. and Y.W. contributed equally to this work. This work was primarily supported by Army Research Office (ARO) under grant W911NF-16-1-0198 and National Science Foundation DMR-1709025. Electron microscopy characterization (P.Z. and P.M.V.) was supported by the Department of Energy, Basic Energy Sciences (DE-FG02-08ER46547) and used facilities supported by the Wisconsin MRSEC (DMR-1720415).

Conflict of Interest

The authors declare no conflict of interest.

Keywords

2D heterostructures, atomic layer deposition, memristors, oxygen vacancies, zinc oxide

Received: February 4, 2020
Revised: March 6, 2020
Published online:

[1] a) S. Goswami, A. J. Matula, S. P. Rath, S. Hedström, S. Saha, M. Annamalai, D. Sengupta, A. Patra, S. Ghosh, H. Jani, S. Sarkar, M. R. Motapothula, C. A. Nijhuis, J. Martin, S. Goswami, V. S. Batista, T. Venkatesan, *Nat. Mater.* **2017**, *16*, 1216; b) J. J. Yang, M. D. Pickett, X. Li, D. A. A. Ohlberg, D. R. Stewart, R. S. Williams, *Nat. Nanotechol.* **2008**, *3*, 429.

[2] a) L. Chua, *IEEE Trans. Circuit Theory* **1971**, *18*, 507; b) D. B. Strukov, G. S. Snider, D. R. Stewart, R. S. Williams, *Nature* **2008**, *453*, 80.

[3] S. Choi, S. H. Tan, Z. Li, Y. Kim, C. Choi, P.-Y. Chen, H. Yeon, S. Yu, J. Kim, *Nat. Mater.* **2018**, *17*, 335.

[4] H. P. Wong, H. Lee, S. Yu, Y. Chen, Y. Wu, P. Chen, B. Lee, F. T. Chen, M. Tsai, *Proc. IEEE* **2012**, *100*, 1951.

[5] J. Choi, J. S. Han, K. Hong, S. Y. Kim, H. W. Jang, *Adv. Mater.* **2018**, *30*, 1704002.

[6] V. K. Sangwan, D. Jariwala, I. S. Kim, K.-S. Chen, T. J. Marks, L. J. Lauhon, M. C. Hersam, *Nat. Nanotechnol.* **2015**, *10*, 403.

[7] A. Chiolerio, I. Roppolo, K. Bejtka, A. Asvarov, C. F. Pirri, *RSC Adv.* **2016**, *6*, 56661.

[8] W.-P. Lin, S.-J. Liu, T. Gong, Q. Zhao, W. Huang, *Adv. Mater.* **2014**, *26*, 570.

[9] M. Laurenti, S. Porro, C. F. Pirri, C. Ricciardi, A. Chiolerio, *Crit. Rev. Solid State Mater. Sci.* **2017**, *42*, 153.

[10] a) A. Mazady, *Doctoral Dissertation*, University of Connecticut, Storrs, CT, USA **2014**, available from: https://opencommons.uconn.edu/dissertations/660; b) K. M. Kim, D. S. Jeong, C. S. Hwang, *Nanotechnology* **2011**, *22*, 254002; c) S. Menzel, M. Waters, A. Marchewka, U. Böttger, R. Dittmann, R. Waser, *Adv. Funct. Mater.* **2011**, *21*, 4487.

[11] R. Ge, X. Wu, M. Kim, J. Shi, S. Sonde, L. Tao, Y. Zhang, J. C. Lee, D. Akinwande, *Nano Lett.* **2018**, *18*, 434.

[12] A. Chiolerio, M. Chiappalone, P. Ariano, S. Bocchini, *Front. Neurosci.* **2017**, *11*.

[13] F. Wang, J.-H. Seo, G. Luo, M. B. Starr, Z. Li, D. Geng, X. Yin, S. Wang, D. G. Fraser, D. Morgan, Z. Ma, X. Wang, *Nat. Commun.* **2016**, *7*, 10444.

[14] a) F. Wang, X. Yin, X. Wang, *Extreme Mech. Lett.* **2016**, *7*, 64; b) X. Yin, Y. Shi, Y. Wei, Y. Joo, P. Gopalan, I. Szlufarska, X. Wang, *Langmuir* **2017**, *33*, 7708.

[15] J. R. Durán Retamal, D. Periyanagounder, J.-J. Ke, M.-L. Tsai, J.-H. He, *Chem. Sci.* **2018**, *9*, 7727.

[16] H.-K. Hong, J. Jo, D. Hwang, J. Lee, N. Y. Kim, S. Son, J. H. Kim, M.-J. Jin, Y. C. Jun, R. Erni, S. K. Kwak, J.-W. Yoo, Z. Lee, *Nano Lett.* **2017**, *17*, 120.

[17] H. Tian, H. Zhao, X.-F. Wang, Q.-Y. Xie, H.-Y. Chen, M. A. Mohammad, C. Li, W.-T. Mi, Z. Bie, C.-H. Yeh, Y. Yang, H. S. P. Wong, P.-W. Chiu, T.-L. Ren, *Adv. Mater.* **2015**, *27*, 7767.

[18] K. Fujiwara, T. Nemoto, M. J. Rozenberg, Y. Nakamura, H. Takagi, *Jpn. J. Appl. Phys.* **2008**, *47*, 6266.

[19] Z. Fang, H. Y. Yu, X. Li, N. Singh, G. Q. Lo, D. L. Kwong, *IEEE Electron Device Lett.* **2011**, *32*, 566.

[20] a) E. J. Yoo, M. Lyu, J.-H. Yun, C. J. Kang, Y. J. Choi, L. Wang, *Adv. Mater.* **2015**, *27*, 6170; b) W.-Y. Chang, Y.-C. Lai, T.-B. Wu, S.-F. Wang, F. Chen, M.-J. Tsai, *Appl. Phys. Lett.* **2008**, *92*, 022110.

[21] C. Li, L. Han, H. Jiang, M.-H. Jang, P. Lin, Q. Wu, M. Barnell, J. J. Yang, H. L. Xin, Q. Xia, *Nat. Commun.* **2017**, *8*, 15666.

[22] V. A. Voronkovskii, V. S. Aliev, A. K. Gerasimova, D. R. Islamov, *Mater. Res. Express* **2019**, *6*, 076411.

[23] R. Pan, J. Li, F. Zhuge, L. Zhu, L. Liang, H. Zhang, J. Gao, H. Cao, B. Fu, K. Li, *Appl. Phys. Lett.* **2016**, *108*, 013504.

[24] a) C.-C. Yeh, H.-W. Zan, O. Soppera, *Adv. Mater.* **2018**, *30*, 1800923; b) N. P. Dasgupta, J. Sun, C. Liu, S. Brittman, S. C. Andrews, J. Lim, H. Gao, R. Yan, P. Yang, *Adv. Mater.* **2014**, *26*, 2137; c) H. Huang, B. Liang, Z. Liu, X. Wang, D. Chen, G. Shen, *J. Mater. Chem.* **2012**, *22*, 13428.

[25] D. B. Strukov, R. S. Williams, *Appl. Phys. A* **2009**, *94*, 515.

[26] C. Zhao, Z. C. Zhao, S. Taylor, R. P. Chalker, *Materials* **2014**, *7*, 5117.

[27] F. M. Simanjuntak, D. Panda, K.-H. Wei, T.-Y. Tseng, *Nanoscale Res. Lett.* **2016**, *11*, 368.

[28] K. Dileep, L. S. Panchakarla, K. Balasubramanian, U. V. Waghmare, R. Datta, *J. Appl. Phys.* **2011**, *109*, 063523.

[29] a) L. Schmidt-Mende, J. L. MacManus-Driscoll, *Mater. Today* **2007**, *10*, 40; b) A. C. Soares Sabioni, *Solid State Ionics* **2004**, *170*, 145.

[30] Y. Li, R. Yao, H. Wang, X. Wu, J. Wu, X. Wu, W. Qin, *ACS Appl. Mater. Interfaces* **2017**, *9*, 11711.

[31] a) Y.-Y. Lin, C.-C. Hsu, M.-H. Tseng, J.-J. Shyue, F.-Y. Tsai, *ACS Appl. Mater. Interfaces* **2015**, *7*, 22610; b) J. Ephraim, D. Lanigan, C. Staller, D. J. Milliron, E. Thimsen, *Chem. Mater.* **2016**, *28*, 5549.

[32] J.-Y. Chen, C.-L. Hsin, C.-W. Huang, C.-H. Chiu, Y.-T. Huang, S.-J. Lin, W.-W. Wu, L.-J. Chen, *Nano Lett.* **2013**, *13*, 3671.

[33] B. Yang, C. Yao, Y. Yu, Z. Li, X. Wang, *Sci. Rep.* **2017**, *7*, 4936.

[34] F.-C. Chiu, P.-W. Li, W.-Y. Chang, *Nanoscale Res. Lett.* **2012**, *7*, 178.

[35] Z. Liu, J. Chou, S. Wei, J. Gan, T. Yew, *IEEE Electron Device Lett.* **2011**, *32*, 1728.

[36] N. Xu, L. F. Liu, X. Sun, C. Chen, Y. Wang, D. D. Han, X. Y. Liu, R. Q. Han, J. F. Kang, B. Yu, *Semicond. Sci. Technol.* **2008**, *23*, 075019.

[37] Y. Han, K. Cho, S. Kim, *Microelectron. Eng.* **2011**, *88*, 2608.

[38] a) C. Lin, C. Tang, S. Wu, S. Yang, Y. Lai, S. Wu, in *The 4th IEEE Int. NanoElectronics Conf.*, IEEE, Piscataway, NJ, USA **2011**, p. 1, https://doi.org/10.1109/INEC.2011.5991798; b) C.-L. Lin, C.-C. Tang, S.-C. Wu, P.-C. Juan, T.-K. Kang, *Microelectron. Eng.* **2015**, *136*, 15.

[39] R. Huang, K. Sun, K. S. Kiang, K. A. Morgan, C. H. de Groot, *Microelectron. Eng.* **2016**, *161*, 7.

[40] D. Xu, Y. Xiong, M. Tang, B. Zeng, *J. Alloys Compd.* **2014**, *584*, 269.

[41] K. C. Sekhar, K. Kamakshi, S. Bernstorff, M. J. M. Gomes, *J. Alloys Compd.* **2015**, *619*, 248.

[42] A. Kumar, M. Das, V. Garg, B. S. Sengar, M. T. Htay, S. Kumar, A. Kranti, S. Mukherjee, *Appl. Phys. Lett.* **2017**, *110*, 253509.

[43] C. Hu, Q. Wang, S. Bai, M. Xu, D. He, D. Lyu, J. Qi, *Appl. Phys. Lett.* **2017**, *110*, 073501.

[44] D. Conti, M. Laurenti, S. Porro, C. Giovinazzo, S. Bianco, V. Fra, A. Chiolerio, C. F. Pirri, G. Milano, C. Ricciardi, *Nanotechnology* **2018**, *30*, 065707.

[45] G. Milano, M. Luebben, Z. Ma, R. Dunin-Borkowski, L. Boarino, C. F. Pirri, R. Waser, C. Ricciardi, I. Valov, *Nat. Commun.* **2018**, *9*, 5151.

[46] F. Song, H. Wang, J. Sun, H. Gao, S. Wu, M. Yang, X. Ma, Y. Hao, *IEEE Electron Device Lett.* **2018**, *39*, 31.

[47] F. M. Simanjuntak, T. Ohno, S. Samukawa, *ACS Appl. Electron. Mater.* **2019**, *1*, 18.